ATLAS NOTE

ATLAS-COM-CONF-2013-036

March 9, 2013

Inclusive cross sections of isolated prompt photons in pp collisions at $\sqrt{s} = 7$ TeV measured with the ATLAS detector using 4.7 fb^{-1} of data

The ATLAS Collaboration

Abstract

A measurement of the cross section for the production of isolated prompt photons in pp collisions at a center-of-mass energy $\sqrt{s} = 7$ TeV is presented. The results are based on an integrated luminosity of 4.7 fb^{-1} collected with the ATLAS detector at the LHC. The cross section is measured as a function of photon transverse energy E_{T}^{γ} in the kinematic range $100 \leq E_{\mathrm{T}}^{\gamma} < 1000$ GeV and in the pseudorapidity regions $|\eta^{\gamma}| < 1.37$ and $1.52 \leq |\eta^{\gamma}| < 2.37$. The results are compared to leading-order parton-shower Monte Carlo models and next-to-leading-order perturbative QCD calculations. Next-to-leading-order perturbative QCD calculations show good agreement with the differential cross sections.

ATLAS-CONF-2013-022
10 March 2013

1 Introduction

Prompt photon production at hadron colliders allows precise tests of perturbative QCD predictions [1] by providing a colorless probe of the hard scattering process. The measurement is sensitive to the gluon content of the proton through the $qg \rightarrow q\gamma$ process, which dominates the prompt photon production cross section at the LHC, and can thus be used to constrain parton distribution functions (PDFs) [2].

Recent measurements of the production cross section of isolated prompt photons have been performed by ATLAS [3, 4] and CMS [5, 6] using pp collision data at $\sqrt{s} = 7$ TeV at the LHC. Earlier measurements were made by CDF and D0 using $p\bar{p}$ collisions collected at $\sqrt{s} = 1.8$ TeV and $\sqrt{s} = 1.96$ TeV at the Tevatron [7, 8, 9, 10].

In this paper, the production cross section of isolated prompt photons is measured in the transverse energy (E_{T}^{γ}) range between 100 GeV and 1 TeV, extending the result of the previous ATLAS measurement [4] which covered the range between 45 GeV and 400 GeV. The differential cross section as a function of E_{T}^{γ} is measured in the pseudorapidity[1] range $|\eta^{\gamma}| < 1.37$ (the barrel region) and $1.52 \leq |\eta^{\gamma}| < 2.37$ (the end-cap region). In these pseudorapidity regions photon reconstruction has a high efficiency and a low background rate. The differential cross section is also studied as a function of η^{γ} for $E_{\mathrm{T}}^{\gamma} > 100$ GeV. The data sample corresponds to an integrated luminosity of 4.71 ± 0.09 fb^{-1} [11]; thus this analysis uses a data set more than two orders of magnitude larger than that used in the previous measurement [4].

In the following, all photons produced in proton–proton collisions and not secondary to hadron decays are considered as "prompt". They include both "direct" photons, which originate from the hard processes calculated in fixed-order perturbation theory, and "fragmentation" photons, which are the result of the soft fragmentation of a colored high p_{T} parton [12, 13]. Photons are considered "isolated" if the transverse energy ($E_{\mathrm{T}}^{\mathrm{iso}}$) within a cone of radius $\Delta R = \sqrt{(\delta\eta)^2 + (\delta\phi)^2} = 0.4$ centered around the photon in the pseudorapidity and azimuthal angle (ϕ) is smaller than 7 GeV. In next-to-leading-order (NLO) parton-level theoretical calculations, $E_{\mathrm{T}}^{\mathrm{iso}}$ is calculated from all partons within the cone, while in the leading-order (LO) parton-shower Monte Carlo (MC) simulations it is calculated from all the generated particles (except muons and neutrinos) inside the cone. Experimentally, $E_{\mathrm{T}}^{\mathrm{iso}}$ is calculated from the energy deposited in the calorimeters in a $\Delta R = 0.4$ cone around the photon candidate, corrected for the effects associated with the energy of the photon candidate itself, the underlying event and the additional pp interactions in the same bunch crossing (pileup) [14]. The main background for the prompt photons consists of photons from decays of light neutral mesons such as the π^0 or η.

2 The ATLAS detector

ATLAS [15] is a multipurpose detector with a forward-backward symmetric cylindrical geometry and nearly 4π coverage in solid angle. The most relevant subdetectors for the present analysis are the inner tracking detector (ID) and the calorimeters.

The ID consists of a silicon pixel detector and a silicon microstrip detector covering the pseudorapidity range $|\eta| < 2.5$, and a straw tube transition radiation tracker covering $|\eta| < 2.0$. It is immersed in a 2 T magnetic field provided by a superconducting solenoid. The ID allows efficient reconstruction of converted photons if the conversion occurs at a radius of less than 0.80 m.

The electromagnetic calorimeter (ECAL) is a lead/liquid-argon (LAr) sampling calorimeter providing coverage for $|\eta| < 3.2$. It consists of a barrel section ($|\eta| < 1.475$) and two end-caps ($1.375 < |\eta| <$

[1] ATLAS uses a right-handed coordinate system with its origin at the nominal interaction point (IP) in the center of the detector, and the z-axis along the beam line. The x-axis points from the IP to the center of the LHC ring, and the y-axis points upwards. Cylindrical coordinates (r, ϕ) are used in the transverse plane, ϕ being the azimuthal angle around the beam line. Observables labelled "transverse" are projected into the $x - y$ plane. The pseudorapidity is defined in terms of the polar angle θ as $\eta = -\ln\tan(\theta/2)$.

3.2). The central region ($|\eta| < 2.5$) is segmented into three longitudinal layers. The first (inner) layer, covering $|\eta| < 1.4$ in the barrel and $1.5 < |\eta| < 2.4$ in the end-caps, has a high η granularity (between 0.003 and 0.006 depending on η), which can be used to provide event-by-event discrimination between single-photon showers and two overlapping showers such as may be produced by π^0 decay. The second layer, which collects most of the energy deposited in the calorimeter by the photon shower, has a cell granularity of 0.025×0.025 in $\eta \times \phi$. The third layer is used to correct high energy showers for leakage. In front of the ECAL a thin presampler layer, covering the pseudorapidity interval $|\eta| < 1.8$, is used to correct for energy loss before the ECAL.

The hadronic calorimeter (HCAL), surrounding the ECAL, consists of an iron/scintillator-tile calorimeter in the range $|\eta| < 1.7$, and two copper/LAr calorimeters spanning $1.5 < |\eta| < 3.2$. The ECAL and HCAL acceptance is extended by two LAr forward calorimeters (using copper and tungsten as absorbers) up to $|\eta| = 4.9$.

A three-level trigger system is used to select events containing photon candidates. The first level (level-1) is implemented in hardware and is based on towers with a coarser granularity (0.1×0.1 in $\eta \times \phi$) than that of the ECAL. They are used to search for electromagnetic deposits in $\eta \times \phi$ regions of 2×1 and 1×2 towers, within a fixed window of size 2×2 and with an E_{T}^{γ} above a programmable threshold. The algorithms of the second and third level triggers (collectively referred to as the *high-level trigger*) are implemented in software. The high-level trigger exploits the full granularity and precision of the calorimeter to refine the level-1 trigger selection, based on improved energy resolution and detailed information on energy deposition in the calorimeter cells.

3 Data and simulated samples

3.1 Collision Data selection

The measurement presented here is based on proton-proton collision data collected at a center-of-mass energy of $\sqrt{s} = 7$ TeV with the ATLAS detector at the LHC in 2011. Only events where both the calorimeter and the ID are fully operational and which have good data quality are used. Events are triggered using a high-level photon trigger, with a nominal E_{T}^{γ} threshold of 80 GeV. The trigger selection criteria on the fraction and profile of the energy measured in the various layers of the calorimeters are looser than the photon identification criteria applied in this analysis; see Section 4.3. For 2011, the average number of pp interactions in the same bunch crossing is nine on average. Events are required to have a reconstructed primary vertex consistent with the average beam-spot position and with at least three associated tracks.

3.2 Simulated events

To study the characteristics of signal and background events, MC samples are generated using `PYTHIA` 6.4 [16], a LO parton-shower MC generator, with the modified LO MRST2007 [17] PDF. The event generator parameters are set according to the ATLAS AMBT2 tune [18]. The ATLAS detector response is simulated using the `GEANT4` program [19]. In order to have a realistic description of the experimental conditions under which the data are taken, pileup interactions are included in the simulation. The pileup in the simulation is tuned to reproduce the distribution of the reconstructed primary vertices per event observed in the analyzed data sample. These samples are then reconstructed with the same algorithms used for data. More details on the event generation and simulation infrastructure of the ATLAS experiment are provided in Ref. [20].

For the study of systematic uncertainties and for comparisons with the final cross sections, events are generated with the `HERWIG` 6.5 [21] model using the ATLAS AUET2 tune [22] and the same PDFs as

used for the PYTHIA event generation. HERWIG and PYTHIA use different parton shower and hadronization models.

Signal MC samples include both hard-scattering photons from the LO processes $qg \to q\gamma$ and $q\bar{q} \to g\gamma$, and photons from QED radiation from quarks produced in QCD $2 \to 2$ processes.

To study background processes, MC samples enriched in photons from meson decays with an $E_{\mathrm{T}}^{\gamma} > 100$ GeV are used. The samples are generated using all tree-level 2→2 QCD processes, removing γ-jet events from quark bremsstrahlung. Events are filtered after event generation by requiring the E_{T}^{γ} in a 0.18×0.18 region in $\eta \times \phi$ at the truth particle level to be greater than 70 GeV.

4 Photon selection

The reconstruction of photons in the ATLAS detector is described in detail elsewhere (see Refs. [23, 24]). The selection of photons is discussed in the following three sections: kinematic preselection, isolation selection and finally shower identification.

4.1 Photon kinematic preselection

As already detailed in Section 3, photon candidates are first required to have passed an 80 GeV trigger. From these, only those with calibrated transverse energies above 100 GeV are retained for the subsequent analysis. The calibration includes an in-situ technique based on the Z boson mass peak [25]. In order to benefit from the fine segmentation of the first layer of the ECAL for identification of genuine prompt photons, the photon candidates should lie within the barrel or the end-cap pseudorapidity regions. After the selection, 2,666,325 photon candidates remain in the data sample.

4.2 Photon isolation selection

Isolation is an important observable for prompt photon studies. The prompt photon signal is expected to be more isolated from hadronic activity than the background. Also, because of the mixture of hard-scattering and fragmentation contributions in the prompt photon signal, it is important to have a well modeled isolation variable that can be linked to the parton-level isolation cut used in NLO QCD computations. A robust isolation prescription will help limit the non-perturbative fragmentation contribution, which is poorly understood in theory, while retaining the signal produced from direct processes.

This study uses the same definition of the cone isolation variable, $E_{\mathrm{T}}^{\mathrm{iso}}$ as for the previous ATLAS measurement [4]. It is computed using calorimeter cells from both the ECAL and HCAL, in a cone of radius $\Delta R = 0.4$ around the photon candidate. The contributions from the 5×7 ECAL cells in the $\eta \times \phi$ space around the photon barycenter are not included in the calculation. The expected small value of the leakage from the photons outside this region, evaluated as a function of the E_{T}^{γ} in simulated samples of single photons, is then subtracted from the isolation variable. The contribution to the photon isolation energy from the underlying event and pileup is subtracted using the procedure proposed in Refs. [26, 27] and implemented as described in Ref. [3]. After these corrections, the transverse isolation energy of simulated prompt photons is independent of the E_{T}^{γ}. A residual mild dependence on in-time pileup (from collisions of protons in the same bunches as the photons produced from the hard scattering) is observed for this isolation variable. This is due to the inconsistent treatment of noise in the calculation of the uncorrected isolation variable. The uncorrected isolation is computed from cells without noise suppression whereas the pileup correction is computed from noise suppressed topological clusters. The pileup dependence of $E_{\mathrm{T}}^{\mathrm{iso}}$ is well modeled in the simulation.

In the following, all photon candidates having reconstructed isolation energies $E_{\mathrm{T}}^{\mathrm{iso}} < 7$ GeV are considered experimentally "isolated", while candidates with $E_{\mathrm{T}}^{\mathrm{iso}} > 7$ GeV are considered "non-isolated".

These definitions are applied to the data and to the MC calculations at both parton and particle level. The isolation requirement $E_{\mathrm{T}}^{\mathrm{iso}} < 7$ GeV is looser than that used in the previous analysis [4]; and is chosen in order to optimize the signal purity and the photon reconstruction efficiency at high E_{T}^{γ}.

4.3 Photon shower-shape identification

Shape variables computed from the lateral and longitudinal energy profiles of the shower in the ECAL are used to further discriminate the signal from the background. The selection criteria do not depend on the photon candidate's transverse energy, but vary as a function of the photon reconstructed pseudorapidity to take into account significant changes in the total thickness of the upstream material and variations in the calorimeter geometry or granularity. The same "tight" selection criteria used in the measurement of the isolated photon-pair production cross section [14] are applied. After the photon identification requirements, 1,329,035 (616,807) photon candidates remain in the barrel (end-cap) η^{γ} region. The fraction of converted photons is 32% (45%) in the barrel (end-cap) η^{γ} region. There are 19 photon candidates with E_{T}^{γ} between 800 GeV and 1 TeV region. The total number of events with more than one good photon candidate after the photon identification requirements is 1240.

5 Background estimation and signal extraction

The main background for prompt photons is due to hadronic jets containing π^0 mesons that carry most of the jet energy and that decay to photon pairs. Such background photons are expected to be less isolated than prompt ones due to activity from the other particles in the jet. The isolation energy, $E_{\mathrm{T}}^{\mathrm{iso}}$, therefore provides a discrimination between prompt photons and photons from jets and meson decays. To avoid relying on the simulation to model accurately the energy flow inside jets and the fragmentation to π^0s, a data-driven technique is used as much as possible in order to extract the background isolation distribution. This requires the selection of an unbiased background-enhanced sample of photon candidates.

Among the shower-shape variables used in the photon selection, some measured in the first ECAL layer are fairly uncorrelated with the $E_{\mathrm{T}}^{\mathrm{iso}}$. A background-enhanced sample is provided by requiring the photon candidates to fail the "tight" identification criteria on at least one of four variables computed from the finely segmented first layer of the calorimeter, and to pass all the other criteria. From now on, such photons will be called "non-tight candidates", while the photon candidates satisfying the "tight" selection will be called "tight candidates".

The residual background contamination in the selected event sample is estimated using the "two-dimensional side bands" method [3]. It is based on the definition of a "tight-isolated" signal region A and three background control regions B, C, D: "tight-non isolated", "non tight-isolated" and "non tight-non isolated", respectively. The basic method assumes that the control regions have negligible signal contamination and that the isolation energy distribution of background events is the same for tight and non-tight candidates. In that case the signal yield in region A, N_S^A, can be obtained from the number N^k of events observed in data, in each of the four regions $k = A$, B, C, and D, as

$$N_S^A = N^A - N^C \frac{N^B}{N^D}. \tag{1}$$

The method can easily be extended to account for deviations from the previous hypotheses, requiring only a limited knowledge of the signal and background properties: in that case, the equation to solve is

$$N_S^A = N^A - R_{\mathrm{BKG}} \frac{(N^B - c_B N_S^A)(N^C - c_C N_S^A)}{(N^D - c_D N_S^A)}, \tag{2}$$

where $c_k = \frac{N^k_{\rm sig}}{N^A_{\rm sig}}$ are the fractions of signal events expected in each of the three control regions, relative to the signal region A, and $R_{\rm BKG} = \frac{N^A_{\rm bkg} N^D_{\rm bkg}}{N^B_{\rm bkg} N^C_{\rm bkg}}$ characterizes the correlation between the isolation and identification variables in background events ($R_{\rm BKG} = 1$ when the correlations are negligible).

Figure 1(a) shows the distribution of $E_{\rm T}^{\rm iso}$ for tight and non-tight candidates. The latter is normalized to the former in the background-dominated region $E_{\rm T}^{\rm iso} > 15$ GeV. The agreement between the two shapes for $E_{\rm T}^{\rm iso} > 15$ GeV reinforces the assumption that a good background estimation can be obtained from the non-tight sample. The excess of tight candidates over normalized non-tight candidates in the region $E_{\rm T}^{\rm iso} < 15$ GeV shows a clear peak for signal prompt photons. Fig. 1(b-c) show the isolation profile of photon candidates after subtracting the distribution of non-tight candidates (with the same normalization as applied in Fig. 1(a)), for different ranges of the photon candidate transverse energy in the two different η^γ regions. The distributions of these signal-enriched samples are largely independent of the $E_{\rm T}^\gamma$ range, as expected from the simulation.

In the following, Eq. (2) is used to estimate the prompt photon yield in the selected sample, with $R_{\rm BKG}$ fixed to 1 as observed (within uncertainties) in simulated background events. Results obtained neglecting signal leakage in the control regions, as in Eq. (1), or with $R_{\rm BKG} \neq 1$ are used to evaluate systematic uncertainties. In the end-cap region the statistics are too low for the 500 to 600 GeV bin, therefore, the signal purity from the preceding bin is used instead.

The MC simulations indicate that the energy resolution of photons in the range $100 < E_{\rm T}^\gamma < 600$ GeV is close to 3%. The widths of the bins for the $E_{\rm T}^\gamma$-differential cross section measurement are chosen to keep the migration between neighboring $E_{\rm T}^\gamma$ bins below 1%. These residual migration effects, which affect the signal purity in a given $E_{\rm T}^\gamma$ bin, are taken into account using corrections based on the signal MC.

Background photons from meson decays are the largest contributing factor to the value of signal purity. Figure 2 shows the signal purity for prompt photons in region A as a function of $E_{\rm T}^\gamma$ for the barrel and end-cap regions. The signal purity is estimated from the data using the two-dimensional side band approach shown in Eq. (1). The shaded bands indicate systematic uncertainties on the signal purity as discussed in Section 8. The measured signal purity is larger than 90% and increases with $E_{\rm T}^\gamma$. The signal purity estimated using the correlated approach shown in Eq. (2) agrees with that using the uncorrelated approach within 4%, and has a similar dependence on $E_{\rm T}^\gamma$.

6 Residual background

A possible residual background could arise from electrons that fake photons; primarily high-$p_{\rm T}$ isolated electrons from W or Z-boson decays that tend to be misidentified as converted photons. This is particularly the case when no hit in the innermost layer of the pixel detector is associated with the electron track and thus the electron is mistakenly assigned to a converted photon vertex. The corresponding misidentification probability is measured by studying the invariant mass spectrum of $e^\pm\gamma$ combinations in the Z mass range. It was found that such contamination is $\approx 0.5\%$ for $E_{\rm T}^\gamma < 400$ GeV [4].

To understand the background from electrons for higher $E_{\rm T}^\gamma$, a MC study was performed using a sample of high-$p_{\rm T}$ electrons. The current analysis neglects contributions from high-$p_{\rm T}$ isolated electrons, since the MC study indicates that the rate of misidentified photons with $E_{\rm T}^\gamma > 500$ GeV originating from electrons is less than 0.5%.

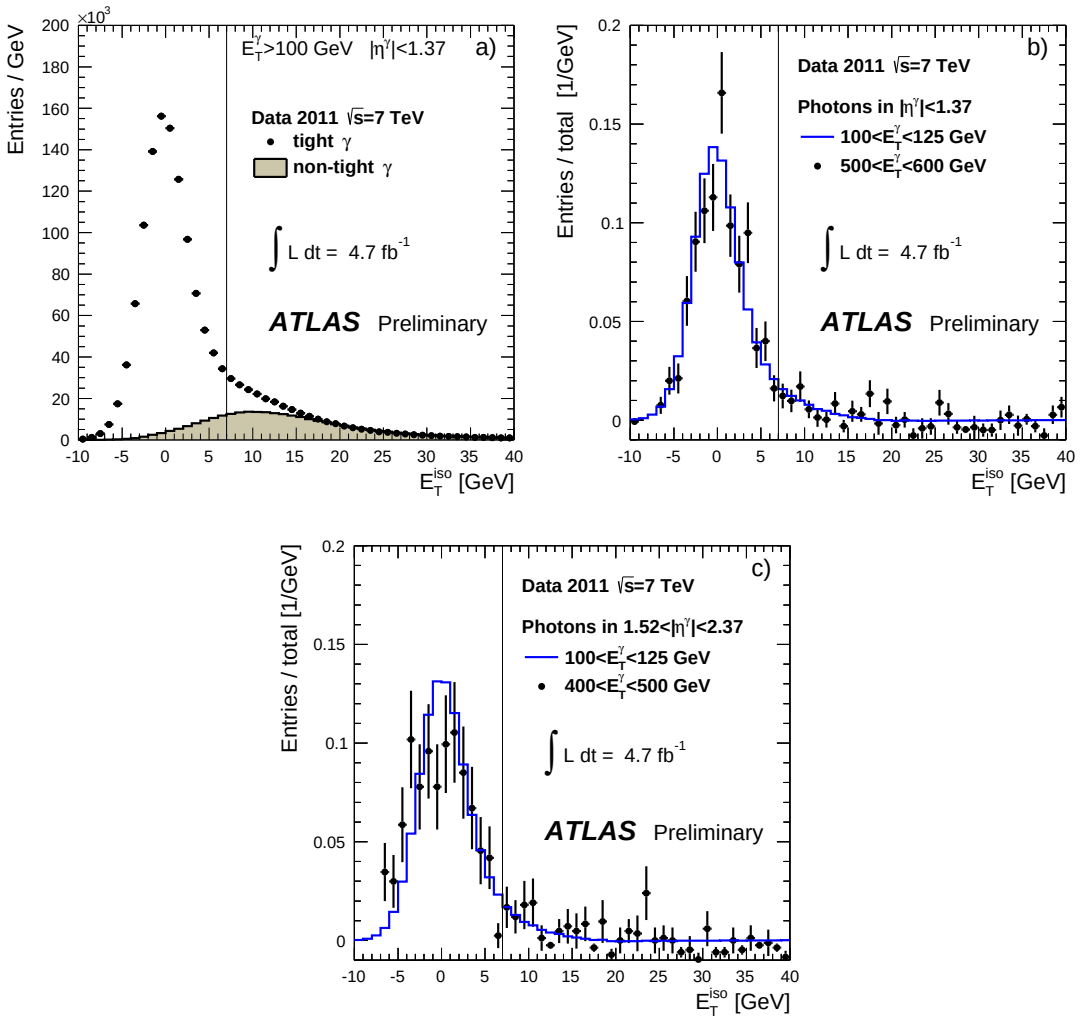

Figure 1: (a): $E_{\mathrm{T}}^{\mathrm{iso}}$ distribution of tight (solid dots) and non-tight (shaded gray region) photon candidates in data, for $E_{\mathrm{T}}^{\gamma} > 100$ GeV for the central η^{γ} region. The latter is normalized to the former for $E_{\mathrm{T}}^{\mathrm{iso}} > 15$ GeV. The excess of tight candidates over the normalized non-tight candidates for $E_{\mathrm{T}}^{\mathrm{iso}} < 15$ GeV shows a clear peak from signal prompt photons. (b)-(c): $E_{\mathrm{T}}^{\mathrm{iso}}$ distributions of tight photons in the barrel and end-cap regions after subtracting the normalized non-tight distribution, for two representative regions with different E_{T}^{γ}. The vertical lines show the requirement $E_{\mathrm{T}}^{\gamma} < 7$ GeV used to define the final cross sections.

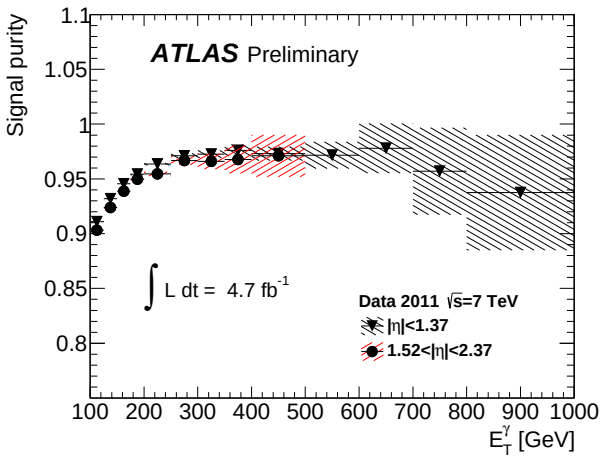

Figure 2: The signal purity for the barrel and end-cap η^{γ} regions estimated from the data using the two-dimensional side band approach shown in Eq. (1). The shaded bands indicate statistical and systematic uncertainties on the signal purity determination as discussed in Section 8.

7 Cross section measurement

The differential cross section for the production of isolated prompt photons in a given phase space bin i is $N_i/(C_i(\gamma)\cdot\Delta_i\cdot\int\mathcal{L}\mathrm{dt})$, where N_i is the number of photons in a bin i after the background subtraction, $C_i(\gamma)$ is a correction factor, Δ_i is the width of bin i and $\int\mathcal{L}\mathrm{dt}$ is the integrated luminosity. The correction factor, $C_i(\gamma)$, is evaluated from the bin-by-bin ratio of the reconstructed and the particle-level prompt photons in the signal simulation. The photon reconstruction in the MC simulation was tuned using data-driven techniques [28]. The correction factor $C_i(\gamma)$ accounts for photon reconstruction and selection efficiency, as well as the event selection efficiency. They are discussed in more detail below:

- Photon reconstruction and selection efficiency. This is the efficiency for a particle level prompt photon, in the acceptance of the differential cross section, to be reconstructed as a photon passing all the photon selection criteria outlined in Section 6. It is determined by using simulated signal events after correcting the simulated calorimeter shower-shapes to match those observed in data [3]. The shower-shape corrections for the MC simulation are determined from the comparison of data with the simulation in the control samples of photons selected in the same kinematic regions as used in this measurement.

- Event selection efficiency. This efficiency includes the trigger efficiency which is defined as the efficiency for an event to pass through a photon trigger with the an energy threshold of 80 GeV. The trigger efficiency is determined using a data-driven technique based on low-E_{T}^{γ} threshold high-level triggers, and it is estimated to be $100^{+0}_{-3}\%$ for $E_{\mathrm{T}}^{\gamma} > 100$ GeV [29].

The average value of the $C_i(\gamma)$ estimated using `PYTHIA` is about 93% for the barrel region and 85% in the end-cap region. It increases with E_{T}^{γ} by approximately 2% in the range of E_{T}^{γ} explored in this measurement.

8 Systematic uncertainties

The systematic uncertainties on the measured differential cross sections are determined by changing the selection or the analysis procedure and repeating the analysis. The systematic variations affect the $C_i(\gamma)$ and signal purity, thus lead to the overall change in the cross section. The largest uncertainties are described below:

- Uncertainty due to discrepancies between the true isolation energy and the reconstructed isolation energy. A typical shift between the true and reconstructed isolation in the MC simulation is less than 1 GeV [4]. The systematic uncertainty on the cross section was estimated by changing the true isolation requirement by ±1 GeV and recalculating the correction factors $C_i(\gamma)$. This systematic variation leads to a typical uncertainty below 2% for all E_{T}^{γ} explored in this measurement.

- A typical shift between data and MC simulation for $E_{\mathrm{T}}^{\mathrm{iso}}$ is less than 0.5 GeV. Therefore, the measurement is repeated by keeping the isolation cut on data at $E_{\mathrm{T}}^{\mathrm{iso}} = 7$ GeV, and varying the isolation threshold by ±0.5 GeV in the MC simulation. This uncertainty is found to be less than 1%, does not depend on E_{T}^{γ}, and is compatible with statistical uncertainty.

- Uncertainty due to photon energy measurement is calculated by varying the photon energy scale within the expected uncertainty in the MC simulation. This uncertainty mostly affects the $C_i(\gamma)$. The effect of such a variation leads to an uncertainty between 2% at low E_{T}^{γ} and 6% at large E_{T}^{γ}.

- Uncertainty on the $C_i(\gamma)$ due to the choice of the MC generator is computed by considering `HERWIG` for the bin-by-bin correction. This uncertainty ranges from 2% at low E_{T}^{γ} to 5% at $E_{\mathrm{T}}^{\gamma} > 800$ GeV.

- Uncertainty on the background subtraction is estimated using alternative background subtraction techniques discussed in Section 5. Eq. (2) is modified to either neglect signal leakage or have $R_{\mathrm{BKG}} \neq 1$. The background is subtracted by either neglecting correlations between the signal and background regions, or using the central values of the correlations estimated from simulated background events. This uncertainty on the cross section varies between 3% and 4% for all E_{T}^{γ} explored in this measurement.

- Uncertainty arising from the definition of the background control regions is estimated by repeating the measurement using an alternative definition of the non-isolated region. The isolation requirement was increased from 7 to 10 GeV. Such definition affects both the signal purity and the correction factor $C_i(\gamma)$. An effect of 1% or less for all E_{T}^{γ} explored in this measurement is observed, which is compatible with statistical uncertainty.

- The measurement is repeated using an alternative definition of the photon transverse isolation energy, based on three-dimensional topological clusters of energy deposits in the calorimeters, affecting mostly the photon reconstruction efficiency. The same calorimeter cells are used for both the calculation of the photon isolation and for the subtraction of the contribution from the underlying event and pileup, thus providing a quantity which is less pileup dependent. A difference smaller than 5% is found between the alternative and the nominal results.

- The systematic uncertainty on the cross section due to the photon energy resolution is calculated by smearing the reconstructed energy in the MC simulations used for the background subtraction and $C_i(\gamma)$. This uncertainty is typically 1% for all E_{T}^{γ} explored in this measurement.

- Uncertainty on the cross section due to insufficient knowledge of the photon reconstruction efficiency is estimated by using different techniques for the photon identification as described in Ref.[28]. An effect of 2% or less for all E_{T}^{γ} explored in this measurement is observed.

- The presence of material in front of the calorimeter affects the photon conversion rate and the development of electromagnetic showers. Therefore the cross section measurement uncertainty depends on the accuracy of the detector simulation. The uncertainty associated with the imperfect knowledge of the material in front of the ECAL was estimated by comparing the measurements using MC samples simulated with the nominal ATLAS setup, and one with increased material. The contribution of this systematic uncertainty on the cross sections was estimated to be 2% on average for all E_{T}^{γ} and increases to 6.5% at $E_{\mathrm{T}}^{\gamma} > 800$ GeV.

- The relative systematic uncertainty on the cross section due to the uncertainty of the luminosity measurement is 1.8%. It is fully correlated among all E_{T} and η bins of the differential cross sections.

The sources of systematic uncertainty are considered uncorrelated and thus the total systematic uncertainty is estimated by summing in quadrature all the contributions.

9 Theoretical predictions

The expected prompt-photon production cross section has been estimated using the JETPHOX 1.3 Monte Carlo program [12, 13], which implements a full NLO QCD calculation of both the direct and fragmentation contributions to the total cross section. The parton-level isolation, defined as the total E_{T} from the partons produced with the photon inside a cone of radius $\Delta R = 0.4$ in $\eta \times \phi$ around the photon direction, is required to be smaller than 7 GeV. The fragmentation contribution in the JETPHOX calculation decreases with increasing E_{T}^{γ} and becomes negligible for $E_{\mathrm{T}}^{\gamma} > 500$ GeV. Further details on the JETPHOX calculation can be found in Ref. [30]. The calculation uses the NLO photon fragmentation function of BFG set II [31]. The CT10 [32] and MSTW2008NLO [33] PDFs for the proton are provided by the LHAPDF package [34]. The nominal renormalization (μ_R), factorization (μ_F) and fragmentation (μ_f) scales have been set to the photon transverse energy ($\mu_R = \mu_F = \mu_f = E_{\mathrm{T}}^{\gamma}$). Systematic uncertainties on the QCD cross sections are estimated in the following way:

- The scale uncertainty is evaluated by varying the three scales following the constraints:
  - $\mu_R = \mu_F = \mu_f \in [E_{\mathrm{T}}^{\gamma}/2, 2E_{\mathrm{T}}^{\gamma}]$;
  - $\mu_R \in [E_{\mathrm{T}}^{\gamma}/2, 2E_{\mathrm{T}}^{\gamma}], \mu_F = \mu_f = E_{\mathrm{T}}^{\gamma}$;
  - $\mu_F \in [E_{\mathrm{T}}^{\gamma}/2, 2E_{\mathrm{T}}^{\gamma}], \mu_R = \mu_f = E_{\mathrm{T}}^{\gamma}$;
  - $\mu_f \in [E_{\mathrm{T}}^{\gamma}/2, 2E_{\mathrm{T}}^{\gamma}], \mu_R = \mu_F = E_{\mathrm{T}}^{\gamma}$;

  This leads to a change of the predicted cross section between 12% and 20%.

- The uncertainty on the differential cross section due to insufficient knowledge of the PDFs was obtained by repeating the JETPHOX calculation for 52 eigenvector sets of the CT10 PDF and applying a scaling factor in order to obtain the uncertainty for the 68% C.L. interval [30]. The corresponding uncertainty on the cross section increases with E_{T}^{γ} and varies between a few % at $E_{\mathrm{T}}^{\gamma} \simeq 100$ GeV and 15% at $E_{\mathrm{T}}^{\gamma} \simeq 900$ GeV.

- The effect of the uncertainty on the value of the strong coupling constant, α_s, is evaluated following the recommendation in Ref. [32]. This was done using different CT10 PDF sets with α_s values varied by ± 0.002 around the central value, $\alpha_s = 0.118$. Then, a scaling factor was applied in order to obtain the uncertainty for the 68% C.L. interval. The average α_s uncertainty on the cross section is 4.5%, with a small dependence on E_{T}^{γ}.

In the following, the total uncertainty will include the three sources above added in quadrature, while the largest uncertainty, due to the scale variation will be shown as a separate band.

In order to perform a correct comparison with the JETPHOX calculation, the effects of hadronization, pileup and underlying events have to be understood because the isolation energy is directly sensitive to these effects. The ambient-energy-density correction used for the $E_{\mathrm{T}}^{\mathrm{iso}}$ reconstruction reduces the effects from underlying events and pileup, but this effect may not be completely taken into account. Using PYTHIA and HERWIG with different tunes, the combined effects from hadronization, pileup and the underlying events is estimated to be at the level of ±2%. This correction is small compared to the full uncertainty from other sources and is not included in the total theoretical uncertainty.

The measured cross sections are also compared to those from the LO parton-shower generators, PYTHIA and HERWIG. These models are described in Section 3.2. Both simulate the fragmentation components through the emission of photons in the parton shower.

10 Results

The differential cross section for the production of isolated prompt photons is obtained from the number of signal events as discussed in Section 7. The measured E_{T}^{γ}-differential cross sections together with the theoretical predictions are shown in Figs. 3 and 4 for the barrel and end-cap η^{γ} regions, respectively. Figure 5 shows the cross section as a function of η^{γ} for $E_{\mathrm{T}}^{\gamma} > 100$ GeV. This cross section is dominated by photons with E_{T}^{γ} close to the threshold cut $E_{\mathrm{T}}^{\gamma} = 100$ GeV. The full error bars on the data points represent the combination of statistical and systematic uncertainties including the luminosity uncertainty (1.8%). The inner error bars show statistical uncertainties. The shaded bands on the NLO predictions show the theoretical uncertainties as discussed in Section 9. The theoretical uncertainties due to the choice of the factorization and renormalization scales are shown as an inner band.

The NLO calculations agree with the data up to the highest E_{T}^{γ} considered. The data are somewhat higher than the central NLO calculation for low E_{T}^{γ}, but agree within the theoretical uncertainty of the NLO calculation. This difference is also consistent throughout η^{γ} as it is dominated by the low E_{T}^{γ} range of the measurement. The central values of the NLO calculation with the MSTW2008NLO PDF agree better with the data for the low E_{T}^{γ} region and lie above the NLO calculation based on the CT10 PDF.

The predictions of the LO parton-shower MC generators, PYTHIA and HERWIG, are also shown in Figs. 3, 4 and 5. The PYTHIA model describes the data, while HERWIG indicates a lower cross section than that observed in the data. Both models describe the shape of the cross sections well.

The data are also compared to MC predictions which include only direct photons from $qg \to q\gamma$ and $q\bar{q} \to g\gamma$ processes calculated at LO QCD. Figure 6 shows that these MC generators predict a 20% lower cross section at low E_{T}^{γ} than when all the higher order fragmentation processes are included. This discrepancy is reduced at high E_{T}^{γ}, where the contribution from soft QCD becomes small. This shows that the higher order fragmentation processes are significant contributions to the shape of the predicted E_{T}^{γ} cross section.

The total inclusive cross section of direct photons calculated in the kinematic region $E_{\mathrm{T}}^{\gamma} > 100$ GeV, $|\eta^{\gamma}| < 1.37$ and $E_{\mathrm{T}}^{\mathrm{iso}} < 7$ GeV is

$$\sigma(\gamma + X) = 234 \pm 2\ (\mathrm{stat})^{+13}_{-9}(\mathrm{syst}) \pm 4\ (\mathrm{lumi})\ \mathrm{pb}.$$

PYTHIA predicts that the cross section is 224 pb while HERWIG predicts 187 pb. The NLO calculations with the CT10 and MSTW2008NLO PDFs predict 203 ± 25 (theory) pb and 212 ± 24 (theory) pb, respectively, where the theory uncertainty is symmetrised and includes the scale, PDF and α_s uncertainties.

The total cross section for direct photons within the kinematic range $E_{\mathrm{T}}^{\gamma} > 100$ GeV, $1.52 \leq |\eta^{\gamma}| < 2.37$ and $E_{\mathrm{T}}^{\mathrm{iso}} < 7$ GeV is

$$\sigma(\gamma + X) = 122 \pm 2\ (\mathrm{stat})^{+9}_{-7}(\mathrm{syst}) \pm 2\ (\mathrm{lumi})\ \mathrm{pb}$$

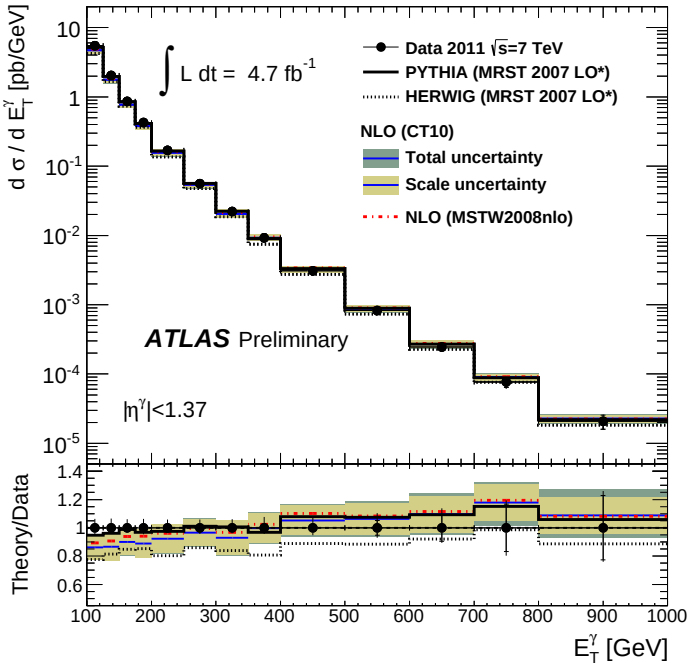

Figure 3: Measured (dots with error bars) and expected inclusive prompt photon cross section in the barrel η^γ region. The inner error bars on the data points show statistical uncertainties, while the full error bars show statistical and systematic uncertainties added in quadrature. The NLO theory prediction is shown as a shaded band which indicates theoretical uncertainties, while the LO parton shower MC generators are shown as lines.

which can be compared to 118 pb (PYTHIA) and 99 pb (HERWIG). The NLO calculations based on CT10 and MSTW2008NLO predict 105 ± 15 (theory) pb and 109 ± 15 (theory) pb, respectively.

11 Conclusion

A measurement of the differential cross sections for the inclusive production of isolated prompt photons in pp collisions at a center-of-mass energy of $\sqrt{s} = 7$ TeV is presented using 4.7 fb^{-1} of collision data collected with the ATLAS detector at the LHC. The cross sections are presented as a function of photon transverse energy E_{T}^{γ} and pseudorapidity η^{γ}. The E_{T}^{γ} kinematic range of this measurement spans from 100 GeV to 1 TeV, thus significantly extending the measured kinematic range previously published [4] by ATLAS. The measured differential cross section falls by more than five orders of magnitude in this kinematic range.

Both PYTHIA and HERWIG describe the shapes of the differential cross sections. The HERWIG generator predicts a smaller cross section compared to PYTHIA and the data. The MC studies presented in this paper indicate that soft QCD processes beyond the LO hard processes are needed for a good description of the data.

The data agree with the NLO predictions based on the CT10 and MSTW2008 PDF up to the highest measured $E_{\mathrm{T}}^{\gamma} \simeq 1$ TeV. In this kinematic regime, the theoretical uncertainties due to the PDF of the proton become significant. Thus the presented cross sections have the potential to provide additional constraints on the proton PDF.

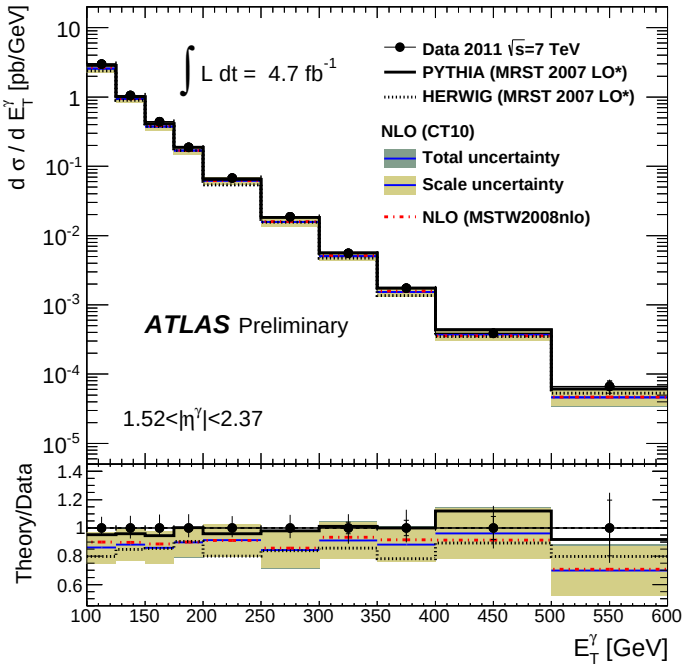

Figure 4: Measured (dots with error bars) and expected inclusive prompt photon cross section in the end-cap η^γ region. The inner error bars on the data points show statistical uncertainties, while the full error bars show statistical and systematic uncertainties added in quadrature. The NLO theory prediction is shown as a shaded band which indicates theoretical uncertainties, while the LO parton shower MC generators are shown as lines.

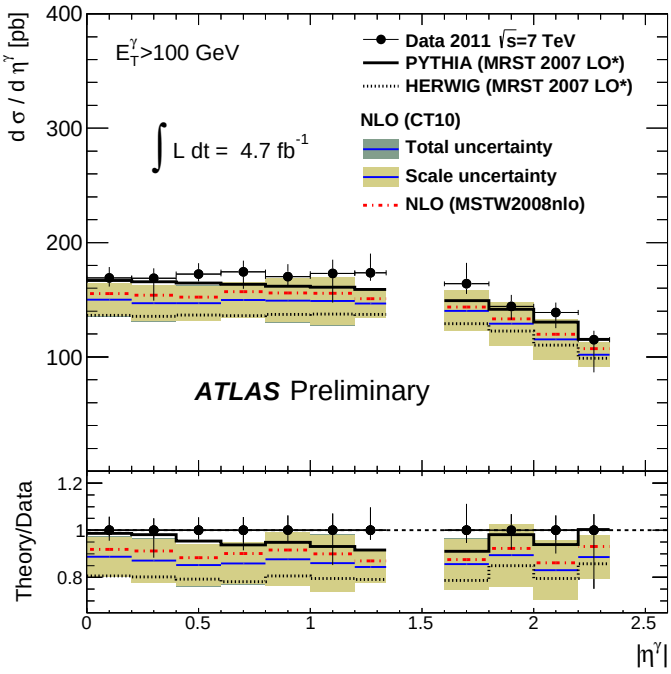

Figure 5: Measured and expected inclusive prompt photon cross section as a function of $|\eta^{\gamma}|$, for photons with transverse energies above 100 GeV excluding $1.37 < |\eta^{\gamma}| < 1.52$. The data points show full error bars which contain statistical, systematic, and luminosity uncertainties added in quadrature. The NLO theory prediction is shown as a shaded band which indicates theoretical uncertainties, while the LO parton shower MC generators are shown as lines.

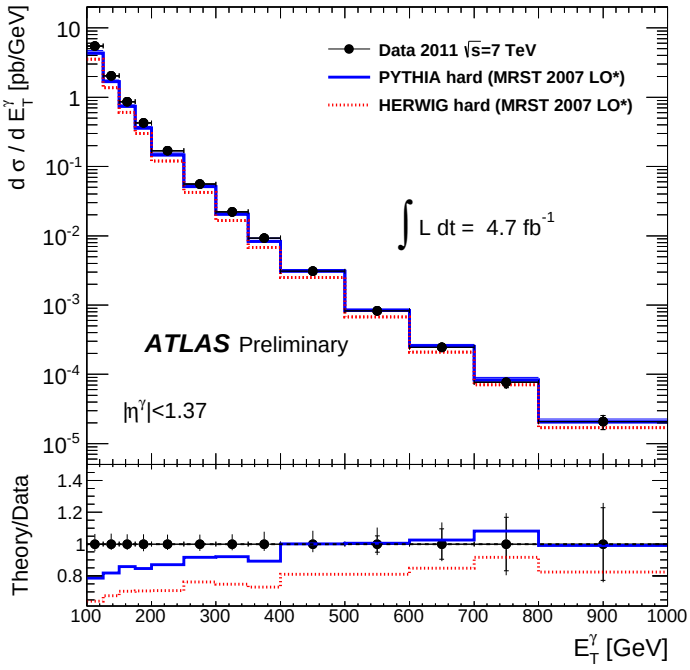

Figure 6: Same data as on Fig. 3, but the comparison is made with MC predictions that include only direct photons from the hard processes.

References

[1] P. Aurenche, R. Baier, M. Fontannaz, and D. Schiff, *Prompt photon production at large p_T. Scheme invariant QCD predictions and comparison with experiment*, Nucl. Phys. **B 297** (1988) 661.

[2] P. Aurenche, R. Baier, M. Fontannaz, J. F. Owens, and M. Werlen, *The gluon content of the nucleon probed with real and virtual photons*, Phys. Rev. **D 39** (1989) 3275.

[3] ATLAS Collaboration, *Measurement of the inclusive isolated prompt photon cross section in pp collisions at $\sqrt{s}$ = 7 TeV with the ATLAS detector*, Phys. Rev. **D 83** (2011) 052005, arXiv:1012.4389 [hep-ex].

[4] ATLAS Collaboration, *Measurement of the inclusive isolated prompt photon cross- section in pp collisions at $\sqrt{s}$ = 7 TeV using 35 pb^{-1} of ATLAS data*, Phys. Lett. **B 706** (2011) 150, arXiv:1108.0253 [hep-ex].

[5] CMS Collaboration, *Measurement of the inclusive isolated prompt photon cross section in pp collisions*, Phys. Rev. Lett. **106** (2011) 082001, arXiv:1012.0799 [hep-ex].

[6] CMS Collaboration, *Measurement of the Differential Cross Section for Isolated Prompt Photon Production in pp Collisions at 7 TeV*, Phys. Rev. **D 84** (2011) 052011, arXiv:1108.2044 [hep-ex].

[7] CDF Collaboration, D. Acosta et al., *Comparison of the isolated direct photon cross sections in $p\bar{p}$ collisions at $\sqrt{s}$ = 1.8-TeV and $\sqrt{s}$ = 0.63-TeV*, Phys. Rev. **D 65** (2002) 112003, arXiv:hep-ex/0201004 [hep-ex].

[8] CDF Collaboration, D. Acosta et al., *Direct photon cross section with conversions at CDF*, Phys. Rev. **D 70** (2004) 074008, arXiv:hep-ex/0404022 [hep-ex].

[9] CDF Collaboration, D. Acosta et al., *Measurement of the inclusive isolated prompt photon cross section in $p\bar{p}$ collisions at $\sqrt{s}$ = 1.96 TeV using the CDF detector*, Phys. Rev. **D 80** (2009) 111106(R), arXiv:0910.3623 [hep-ex].

[10] D0 Collaboration, V. Abazov et al., *Measurement of the isolated photon cross section in $p\bar{p}$ collisions at $\sqrt{s}$ = 1.96-TeV*, Phys. Lett. **B 639** (2006) 151, arXiv:051.1054 [hep-ex].

[11] ATLAS Collaboration, *Improved luminosity determination in pp collisions at $\sqrt{s}$ = 7 TeV using the ATLAS detector at the LHC*, Tech. Rep. CERN-PH-EP-2013-026, 2013. arXiv:1302.4393 [hep-ex]. http://cds.cern.ch/record/1517411.

[12] S. Catani et al., *Cross section of isolated prompt photons in hadron-hadron collisions*, JHEP **05** (2002) 028, arXiv:hep-ph/0204023 [hep-ph].

[13] P. Aurenche, M. Fontannaz, J.-P. Guillet, E. Pilon, and M. Werlen, *A New critical study of photon production in hadronic collisions*, Phys. Rev. **D 73** (2006) 094007, arXiv:hep-ph/0602133.

[14] ATLAS Collaboration, *Measurement of isolated-photon pair production in pp collisions at $\sqrt{s}$ = 7 TeV with the ATLAS detector*, arXiv:1211.1913 [hep-ex].

[15] ATLAS Collaboration, *The ATLAS Experiment at the CERN Large Hadron Collider*, JINST **3** (2008) S08003.

[16] T. Sjöstrand, S. Mrenna, and P. Z. Skands, *PYTHIA 6.4 Physics and Manual*, JHEP **05** (2006) 026.

[17] A. Sherstnev and R. S. Thorne, *Parton distributions for LO generators*, Eur. Phys. J. **C 55** (2008) 553.

[18] ATLAS Collaboration, *ATLAS tunes of PYTHIA 6 and Pythia 8 for MC11*, ATL-PHYS-PUB-2011-009, 2011. http://cds.cern.ch/record/1363300.

[19] GEANT4 Collaboration, S. Agostinelli et al., GEANT4 - *a simulation toolkit*, Nucl. Instrum. Methods **A 506** (2003) 250.

[20] ATLAS Collaboration, *The ATLAS Simulation Infrastructure*, Eur. Phys. J. **C 70** (2010) 823, arXiv:1005.4568 [physics.ins-det].

[21] G. Corcella et al., *HERWIG 6: An Event generator for hadron emission reactions with interfering gluons (including supersymmetric processes)*, JHEP **0101** (2001) 010, arXiv:hep-ph/0011363 [hep-ph].

[22] ATLAS Collaboration, *New ATLAS event generator tunes to 2010 data*, ATL-PHYS-PUB-2011-008, 2011. http://cds.cern.ch/record/1345343.

[23] ATLAS Collaboration, *Electron and photon reconstruction and identification in ATLAS: expected performance at high energy and results at 900 GeV*, ATLAS-CONF-2010-005, 2010. http://cds.cern.ch/record/1273197/.

[24] ATLAS Collaboration, *Expected Performance of the ATLAS Experiment, Detector, Trigger and Physics*. CERN-OPEN-2008-020, Geneva, 2009. arXiv:0901.0512 [hep-ex]. http://cds.cern.ch/record/1125884.

[25] ATLAS Collaboration, *Electron performance measurements with the ATLAS detector using the 2010 LHC proton-proton collision data*, Eur. Phys. J. **C 72** (2012) 1909, arXiv:1110.3174 [hep-ex].

[26] M. Cacciari, G. P. Salam, and G. Soyez, *The Catchment Area of Jets*, JHEP **04** (2008) 042.

[27] M. Cacciari, G. P. Salam, and S. Sapeta, *On the characterisation of the underlying event*, JHEP **04** (2010) 065, arXiv:0912.4926 [hep-ph].

[28] ATLAS Collaboration, *Measurements of the photon identification efficiency with the ATLAS detector using 4.9 fb^{-1} of pp collision data collected in 2011*, ATLAS-CONF-2012-123 (2012) . http://cdsweb.cern.ch/record/1473426/.

[29] ATLAS Collaboration, *Performance of the Electron and Photon Trigger in p-p Collisions at $\sqrt{s}$=7 TeV with the ATLAS Detector at the LHC in 2011*, ATLAS-CONF-2012-048, 2012. http://cds.cern.ch/record/1450089.

[30] R. Blair et al., *NLO Theoretical Predictions for Photon Measurements Using the PHOX Generators*, CERN-OPEN-2011-041, Sep, 2011. http://cds.cern.ch/record/1379880.

[31] L. Bourhis, M. Fontannaz, and J. Guillet, *Quark and gluon fragmentation functions into photons*, Eur. Phys. J. **C2** (1998) 529, arXiv:hep-ph/9704447.

[32] H.-L. Lai et al., *New parton distributions for collider physics*, Phys. Rev. **D 82** (2010) 074024, arXiv:1007.2241 [hep-ph].

[33] A. Martin, W. Stirling, R. Thorne, and G. Watt, *Parton distributions for the LHC*, Eur. Phys. J. **C 63** (2009) 189, arXiv:0901.0002 [hep-ph].

[34] W. Giele, E. N. Glover, I. Hinchliffe, J. Huston, E. Laenen, et al., *The QCD / SM working group: Summary report*, arXiv:hep-ph/0204316 [hep-ph].